The Lorenz energy cycle in simulated rotating annulus flows

R. M. B. Young

Citation: Physics of Fluids (1994-present) **26**, 056602 (2014); doi: 10.1063/1.4873921
View online: http://dx.doi.org/10.1063/1.4873921
View Table of Contents: http://scitation.aip.org/content/aip/journal/pof2/26/5?ver=pdfcov
Published by the AIP Publishing

PHYSICS OF FLUIDS **26**, 056602 (2014)

The Lorenz energy cycle in simulated rotating annulus flows

R. M. B. Young[a)]

Atmospheric, Oceanic and Planetary Physics, Department of Physics, University of Oxford, Oxford, United Kingdom

(Received 13 February 2014; accepted 17 April 2014; published online 7 May 2014)

Lorenz energy cycles are presented for a series of simulated differentially heated rotating annulus flows, in the axisymmetric, steady, amplitude vacillating, and structurally vacillating flow regimes. The simulation allows contributions to the energy diagnostics to be identified in parts of the fluid that cannot be measured in experiments. These energy diagnostics are compared with laboratory experiments studying amplitude vacillation, and agree well with experimental time series of kinetic and potential energy, as well as conversions between them. Two of the three major energy transfer paradigms of the Lorenz energy cycle are identified—a Hadley-cell overturning circulation, and baroclinic instability. The third, barotropic instability, was never dominant, but increased in strength as rotation rate increased. For structurally vacillating flow, which matches the Earth's thermal Rossby number well, the ratio between energy conversions associated with baroclinic and barotropic instabilities was similar to the measured ratio in the Earth's mid-latitudes. © *2014 AIP Publishing LLC*. [http://dx.doi.org/10.1063/1.4873921]

I. INTRODUCTION

In atmospheric science the instabilities and imbalances driving fluid flow are often presented as an exchange of energy between the potential energy associated with a fluid's temperature or specific entropy, and the kinetic energy associated with its velocity. The potential energy available for conversion to kinetic energy is called the *available potential energy*, and represents the energy that can be converted to kinetic energy by adiabatic redistribution of mass, without any change in the internal energy of the fluid.[1] The basic atmospheric cycle between available potential and kinetic energy was presented by Lorenz.[1] James[2] lists the energy exchanges defining three paradigms of the atmospheric general circulation: an overturning (Hadley-type) circulation, barotropic, and baroclinic instabilities (Fig. 5.14 of Ref. 2). The Lorenz energy cycle is now part of the standard textbook description of the basic processes underlying atmospheric flow.[2,3]

The Lorenz energy cycle has also been used to study energy exchanges in the differentially heated rotating annulus, a laboratory experiment used to reproduce the salient features of a planetary atmosphere—gravity, rotation, and differential heating between low and high latitudes—under laboratory conditions. Pfeffer and Chiang,[4] and later Pfeffer, Buzyna, and Fowlis[5] (hereafter P74), presented laboratory studies of the energy cycle in the amplitude vacillating regime. Ukaji and Tamaki[6–9] examined energy exchanges in annulus flows using experiments but also with numerical simulations, for the case where the annulus has a free-slip upper boundary.

The major advantage of the numerical simulation approach is that it allows us to "observe" all parts of the fluid at once, and obtain both temperature and velocities (in three directions) at the same time. Laboratory experiments are generally restricted to measuring either temperature or velocity, and then only at a limited number of points, only in one plane of the fluid, and usually

a)Electronic mail: young@atm.ox.ac.uk

excluding the boundary layers. This paper presents an overview of the energy exchanges taking place within the four major flow regimes observed using the classical rotating annulus setup, as simulated numerically. The simulated environment is particularly useful for such diagnostics, as the full vertical plane can be "observed" at once, including the boundary layers; this gives us the azimuthal means required for the various energy terms and exchanges.

II. SIMULATIONS

Four simulations were run differing only in rotation rate, Ω, covering the four main flow regimes obtained in the differentially heated rotating annulus experiment.[11,12]

Each run used conducting inner and outer cylinders at temperatures $T_a = 18^{\circ}$C and $T_b = 22^{\circ}$C, respectively, i.e., a temperature difference of $\Delta T = 4^{\circ}$C between the cylinders, and insulating no-slip top and bottom boundaries. The fluid, dimensions, and model were identical to that used by Young and Read:[13] annulus inner and outer cylinders at $a = 2.5$ cm and $b = 8$ cm, respectively, annulus depth $d = 14$ cm, and fluid with Prandtl number $Pr = 13.4$ (a mixture of 17% glycerol/83% water by volume).

The numerical model used was the Met Office/Oxford Rotating Annulus Laboratory Simulation (MORALS),[14,15] which solves the Boussinesq Navier-Stokes, continuity, and heat equations for a rotating fluid annulus in cylindrical polar coordinates. The equations are expressed in temperature-velocity form (radial u, azimuthal v, and vertical w velocities, and "azimuthal" and "zonal" will be used interchangeably) in cylindrical polar coordinates (R, ϕ, z). A more detailed technical description of the model was given by Young and Read,[13] along with the full model equations. The technical setup of the model was identical to the setup described there, except in these simulations 32 radial, 128 azimuthal, and 32 vertical grid points were used, with a time step of $\delta t = 0.005$ s. The model grid is stretched to resolve the boundary layers better, with three grid points across each boundary layer.

Each of the four simulations ran for 5000 s of simulated time. This was sufficient for each simulation to equilibrate to a single flow regime, plus several complete periods of any characteristic cycles (e.g., the amplitude vacillation cycle) once equilibrium was attained. Table I lists the simulations and flow regimes, and Fig. 1 shows the basic horizontal and vertical appearance of the flow after 4500 s in each case.

All four regimes contain strong overturning flow in the boundary layers, rising at the outer cylinder and falling at the inner cylinder. The azimuthal flow is prograde in the top half of the domain, and retrograde in the bottom half. The AX regime is azimuthally symmetric with strong azimuthal flow in both directions. The S regime contains a baroclinic wave whose amplitude remains constant over time and drifts around the tank in the prograde direction. The AV regime is similar to the S regime but the amplitude of the baroclinic wave oscillates periodically in time. Finally, the amplitude of the baroclinic wave in the SV regime remains approximately constant, but the shape of the wave varies (typically irregularly) over time. Additional runs (not shown) showed that the transition between the regular wave and weak wave regimes (a regime between axisymmetric flow and full baroclinic flow with waves of relatively weak amplitude—typically 10% of full baroclinic flow) occurs around $\Omega = 0.49$ rad s^{-1} or $Ro_T = 2.1$. This transition point is quite a strong function of *Ta* and wavenumber (see, e.g., Hignett *et al.*,[14] Fig. 2).

TABLE I. List of simulations. *Ta* and Ro_T are defined in Read[10] (Eqs. (1) and (2)). The numerical prefix for each identifier is the wavenumber of the dominant wave.

Identifier	AX	2AV	3S	3SV
Flow regime	Axisymmetric	Amplitude vacillation	Steady flow	Structural vacillation
Rotation rate Ω (rad s^{-1})	0.30	0.52	1.40	3.00
Taylor number *Ta*	4.4×10^5	1.3×10^6	9.6×10^6	4.4×10^7
Thermal Rossby number Ro_T	5.6	1.9	0.26	0.056

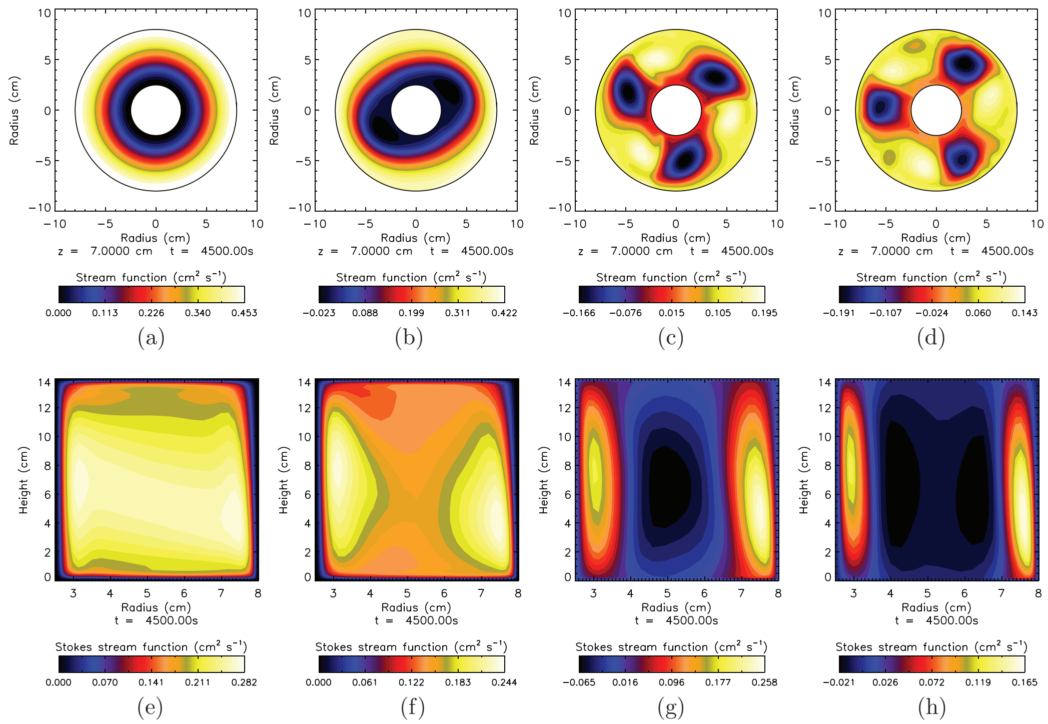

FIG. 1. Basic horizontal appearance of the flow after 4500 s at mid-height, shown as horizontal stream functions ψ defined by $\mathbf{u} = \hat{\mathbf{z}} \times \nabla\psi$ (top, black/blue is cyclonic [dark in print]), and vertical appearance shown as meridional (Stokes) stream functions Ψ of the zonal mean flow, defined by $R\overline{\mathbf{u}} = -\hat{\phi} \times \nabla\Psi$ (bottom, yellow/white is anticlockwise [light in print]). Note that, for practical reasons, the axis scalings in (e)–(h) do not preserve the R-z aspect ratio of the real annulus. This is done throughout the paper. (a) AX, horizontal. (b) 2AV, horizontal. (c) 3S, horizontal. (d) 3SV, horizontal. (e) AX, vertical. (f) 2AV, vertical. (g) 3S, vertical. (h) 3SV, vertical.

III. ENERGY DIAGNOSTICS

The energy diagnostics are based on the Lorenz[1] energy cycle. There are four energy types, the zonal (Z) and eddy (E) components of kinetic (K) and available potential (A) energy, along with energy exchanges between them (C). The complete energy cycle is shown schematically in Fig. 2.

A field $x(R, \phi, z, t)$ can be decomposed into zonal and eddy (non-zonal) components by $x(R, \phi, z, t) = \overline{x}(R, z, t) + x'(R, \phi, z, t)$, or into a horizontal mean and the deviation from that mean by $x(R, \phi, z, t) = \tilde{x}(z, t) + x''(R, \phi, z, t)$. Taking the zonal average of this equation one can also write $\overline{x}(R, z, t) = \tilde{x}(z, t) + \overline{x}''(R, z, t)$.

P74 presented expressions for the Lorenz[1] energy types and exchanges in the differentially heated rotating annulus context (Eqs. (4)–(8)). The equations for the energy types and exchanges are reproduced from P74 below. Here u and v are swapped from the original, to be consistent with previous work using MORALS (u is radial velocity, positive outwards, and v is zonal/azimuthal

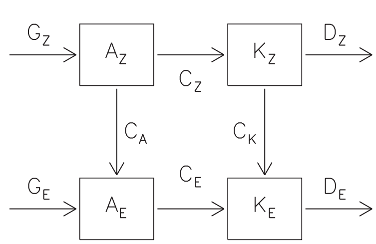

FIG. 2. Schematic of the Lorenz energy cycle, showing the directions of energy transfer when the quantities defined in Eqs. (5)–(8) and Eqs. (14)–(17) are positive.

velocity, positive anticlockwise). A minor correction to the C_A term is applied.[16] Finally, unlike the atmosphere, in the annulus typical vertical velocities are comparable with horizontal velocities, so additional terms involving vertical velocity are included in the kinetic energy types (K_Z and K_E) and exchange (C_K), taken from Ukaji and Tamaki,[6] pp. 363–364. These were omitted from both Lorenz[1] and P74:

$$A_Z \equiv \frac{g\alpha}{2V} \iint \frac{(\overline{T}'')^2}{\partial \tilde{T}/\partial z} R\, dR\, dz, \tag{1}$$

$$A_E \equiv \frac{g\alpha}{2V} \iint \frac{\overline{(T')^2}}{\partial \tilde{T}/\partial z} R\, dR\, dz, \tag{2}$$

$$K_Z \equiv \frac{1}{2V} \iint (\overline{u}^2 + \overline{v}^2 + \overline{w}^2) R\, dR\, dz, \tag{3}$$

$$K_E \equiv \frac{1}{2V} \iint [\overline{(u')^2} + \overline{(v')^2} + \overline{(w')^2}] R\, dR\, dz, \tag{4}$$

$$C_Z \equiv (A_Z \to K_Z) \equiv \frac{g\alpha}{V} \iint \overline{w}''\overline{T}'' R\, dR\, dz \tag{5}$$

$$C_E \equiv (A_E \to K_E) \equiv \frac{g\alpha}{V} \iint \overline{w'T'} R\, dR\, dz, \tag{6}$$

$$C_A \equiv (A_Z \to A_E) \equiv -\frac{g\alpha}{V} \iint \frac{1}{\partial \tilde{T}/\partial z} \left(\overline{T'u'} \frac{\partial \overline{T}''}{\partial R} + \overline{T'w'}'' \frac{\partial \overline{T}''}{\partial z} \right) R\, dR\, dz, \tag{7}$$

$$\begin{aligned} C_K \equiv (K_Z \to K_E) \equiv -\frac{1}{V} \iint \Bigg[& R \left(\overline{u'v'} \frac{\partial}{\partial R} + \overline{v'w'} \frac{\partial}{\partial z} \right) \frac{\overline{v}}{R} \\ & + R \left(\overline{u'u'} \frac{\partial}{\partial R} + \overline{u'w'} \frac{\partial}{\partial z} + \frac{\overline{u'^2} + \overline{v'^2}}{R} \right) \frac{\overline{u}}{R} \\ & + \left(\overline{u'w'} \frac{\partial}{\partial R} + \overline{w'w'} \frac{\partial}{\partial z} \right) \overline{w} \Bigg] R\, dR\, dz, \end{aligned} \tag{8}$$

where

$$V = \iint R\, dR\, dz = \frac{1}{2}(b^2 - a^2)d. \tag{9}$$

These quantities were evaluated every $\Delta t = 20\,\mathrm{s}$ between $t = 3000$ and 5000 s. All derivatives were estimated using quadratic Lagrangian interpolation.[17] From the rate of change of each energy diagnostic, the following equations can be written down for the available potential energy generation (G) and kinetic energy dissipation (D) terms:

$$\frac{dA_Z}{dt} = G_Z - C_Z - C_A, \tag{10}$$

$$\frac{dK_Z}{dt} = C_Z - C_K - D_Z, \tag{11}$$

$$\frac{dA_E}{dt} = G_E + C_A - C_E, \tag{12}$$

$$\frac{dK_E}{dt} = C_E + C_K - D_E. \tag{13}$$

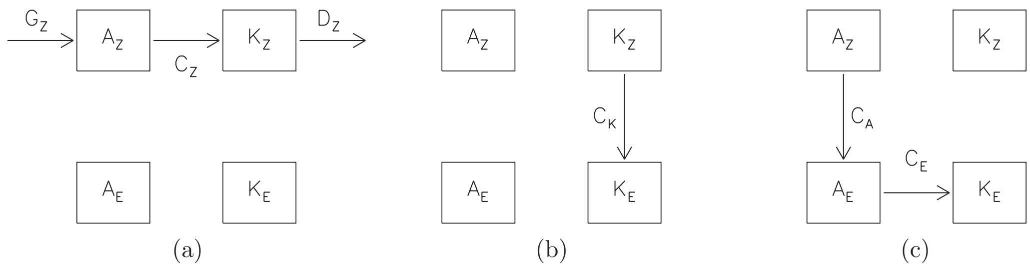

FIG. 3. Paradigms of the Lorenz energy cycle identified by James.[2] (a) Hadley cycle. (b) Barotropic instability. (c) Baroclinic instability.

Rearranging these the generation and dissipation terms are

$$G_Z = C_Z + C_A + \frac{dA_Z}{dt}, \tag{14}$$

$$D_Z = C_Z - C_K - \frac{dK_Z}{dt}, \tag{15}$$

$$G_E = C_E - C_A + \frac{dA_E}{dt}, \tag{16}$$

$$D_E = C_E + C_K - \frac{dK_E}{dt}. \tag{17}$$

James[2] identified three paradigms of the Lorenz energy cycle associated with particular types of atmospheric flow (Fig. 5.14 of Ref. 2). Axisymmetric Hadley circulation has positive G_Z, C_Z, and D_Z. Barotropic instability has positive C_K, and baroclinic instability has positive C_A and C_E. These are shown in Fig. 3.

The Lorenz energy cycle does have some limitations in this context, as it assumes static stability and hydrostatic balance. Formally the model is non-hydrostatic, and typically admits solutions that are statically unstable in the top and bottom (endwall) boundary layers. In practice the difference this makes to the integrated energy diagnostics is very small, as the area covered by the endwall boundary layers is a small percentage (typically 1%) of the total in the integrals. Nevertheless, the reader should be aware of the limitations of this formulation.

IV. RESULTS

A. Energy cycles

Complete energy cycles, which summarise all the energy transfers associated with the flow at a particular time, are presented in Fig. 4 for the flow at 4500 s. This time was chosen as it is approximately halfway between the maximum and minimum of the amplitude vacillation cycle in the 2AV case.

In the AX case (Fig. 4(a)), the Hadley circulation is clear. All the energy types and transfers associated with the eddy fields are zero within floating point precision, as expected for an axisymmetric flow. All that remains is the energy transfer from zonal available potential energy to zonal kinetic energy, associated with the overturning circulation.

Figures 4(b)–4(d) are in order of increasing Ω, or decreasing Ro_T, so the tendency towards baroclinic instability may be expected to increase as one moves through the figure. Baroclinic instability is typically associated with the energy flow $A_Z \rightarrow A_E \rightarrow K_E$. As Ω increases, one might expect more energy to be diverted along the C_A branch compared with the C_Z branch. Because of the differential heating, however, there is always a strong overturning circulation associated with the boundary layers (e.g., Fig. 1(e)). So one expects C_Z to remain appreciably large, even when baroclinic

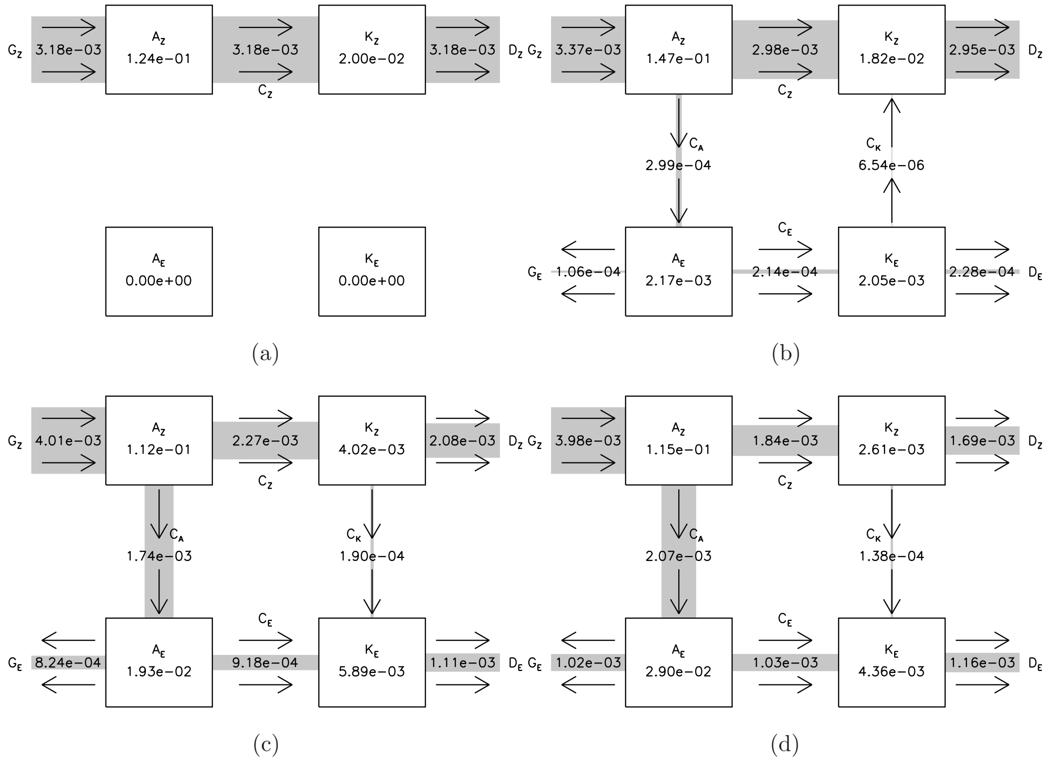

FIG. 4. The energy cycles at $t = 4500$ s for the four simulations. All energy types (in boxes) are in cm^2 s^{-2} ($\equiv 10^{-4}$ J kg^{-1}) and all energy transfers (arrows) are in cm^2 s^{-3} ($\equiv 10^{-4}$ W kg^{-1}). Energy transfers below floating-point precision (10^{-18}) are omitted, and energy types below this value are displayed as zero. (a) AX. (b) 2AV. (c) 3S. (d) 3SV.

instability is strong. This is somewhat different from the situation in the Earth's mid-latitudes, where the heated cylinders do not have a direct analogue, and the meridional overturning circulation is weak compared with the near-equatorial region characterised by the Hadley cell (Read[10], Fig. 1(c)). The three cases with wave structures, 2AV, 3S, and 3SV, exhibit the expected energy transfer terms associated with baroclinic instability. As Ω increases, these terms become stronger, confirming the increasing dominance of baroclinic instability. Table II presents a number of ratios summarising the relative strengths of the various energy transfer terms. The strength of baroclinic instability relative to the overturning circulation is characterised by $C_A : C_Z$. The table clearly shows this ratio increases with Ω, and hence the tendency towards baroclinic instability increases at the expense of the overturning circulation.

In all cases the tendency towards barotropic instability, C_K, is small compared with the baroclinic tendency C_A. The ratio of these two terms is also presented in Table II. The trend in C_K is positive with Ω, corresponding to an increasing strength of barotropic instability with rotation. Lorenz[1] stated that over the Earth's northern hemisphere, the ratio $C_A : C_K$ is about 20, and the values obtained in the

TABLE II. Ratios between various energy transfer terms for the four runs using the data between $t = 3000$ and 5000 s. The value displayed is the median over this period with the interquartile range in sub/superscripts. The supplementary material[23] contains plots of these ratios as time series.

Regime	$C_A : C_Z$	$C_A : C_K$	$G_Z : C_A$
AX	Small ($C_A \approx 0$)	N/A (both ≈ 0)	Large ($C_A \approx 0$)
2AV	$0.0529^{+0.1191}_{-0.0354}$	$-54.4^{+9.9}_{-5.6}$	$21.3^{+39.8}_{-14.2}$
3S	$0.769^{+0.000}_{-0.000}$	$9.19^{+0.0}_{-0.0}$	$2.30^{+0.00}_{-0.00}$
3SV	$1.16^{+0.06}_{-0.04}$	$15.0^{+1.2}_{-0.5}$	$1.87^{+0.06}_{-0.08}$

TABLE III. Amount of energy available compared with the Earth's atmosphere. The first column estimates the ratio of available to total potential energy. Approximate values for the Earth's atmosphere are from Lorenz.[1] Sub/superscripts are as Table II.

Regime	$\left[(\overline{T}'')^2 + \overline{(T')^2}\right] : \overline{T}^2$ (%)	$K : A$ (%)	$K_E : A_E$ (%)
AX	$1.38^{+0.00}_{-0.00} \times 10^{-4}$	$16.1^{+0.0}_{-0.0}$	N/A
2AV	$2.11^{+0.05}_{-0.14} \times 10^{-4}$	$15.1^{+0.1}_{-0.8}$	$90.4^{+4.4}_{-2.5}$
2S	$1.83^{+0.00}_{-0.00} \times 10^{-4}$	$7.52^{+0.00}_{-0.00}$	$30.5^{+0.0}_{-0.0}$
3SV	$2.23^{+0.06}_{-0.04} \times 10^{-4}$	$5.08^{+0.22}_{-0.17}$	$15.4^{+0.4}_{-0.4}$
Earth's atmosphere	0.5	10	50

various wave flow runs are within $O(1)$ of this. The ratio for the 3SV case is closest to 20, which is encouraging as the 3SV case is closest to Earth's mid-latitudes as measured by Ro_T (approximately 0.11 for Earth[18,19]).

Lorenz[1] also discussed the ratio between the generation term G_Z and the potential energy conversion term C_A, which are about equal for the Earth's mid-latitudes. This identity is also satisfied within $O(1)$ for the 3S and 3SV flows (again, with the 3SV case matching Earth's value better). It is not met as well in the 2AV flow, but this flow differs considerably from Earth in terms of Ro_T and hence the tendency towards baroclinic instability characterised by C_A. G_Z, primarily a function of ΔT, remains approximately constant for the four flow regimes.

Lorenz also provided a possible explanation for the intriguing eddy generation terms G_E. At first glance one might expect these to be positive (i.e., adding to the eddy available potential energy). However, they are negative in the three cases with wave flow. In each case the energy flux to eddy kinetic energy (C_E) exceeds the negative eddy generation term, but it is non-negligible, being close to G_E in the 3S and 3SV cases. He suggested that G_E should not necessarily be expected to be positive, because cold air masses will be warmed and warm air masses cooled in mid-latitudes.

Finally, the potential energy available for conversion to kinetic energy and the energy actually converted can be compared with values for the Earth's atmosphere presented by Lorenz.[1] Table III summarizes these numbers for the annulus simulations. In the Earth's atmosphere about 0.5% of the total potential energy is available, and of that about 10% is actually converted to kinetic, rising to 50% considering eddies alone. In the annulus simulations the fraction of total potential energy that is available can be estimated by averaging the ratio $[(\overline{T}'')^2 + \overline{(T')^2}] : \overline{T}^2$ over the domain. This fraction is much smaller than in the Earth's atmosphere: the mean temperature in the annulus is similar to the Earth's surface, but the temperature fluctuations are much smaller (typically 0.15°C compared with 15°C for the Earth[1]). However, both the fraction of available potential energy converted to kinetic energy and the fraction for the eddies alone are similar to the atmospheric values.

B. Time series

Figure 5 shows how the various energy types and transfers vary over time. Only the 2AV and 3SV cases are plotted, because all the lines on the AX and 3S plots are flat (within round-off error) with values given in their respective cycles in Fig. 4. The 3SV plots are approximately flat, varying within a few percent of the mean over that regime's (shape) vacillation cycle, which is about 200 s long. In the 3SV regime the vacillation is in the shape of the baroclinic waves at approximately constant amplitude, which leads to an approximately flat set of energy diagnostics. There is still some structure in these time series, however, which will be discussed below.

1. Amplitude vacillation

In the 2AV case there is considerable variation in the diagnostics over the vacillation cycle (about 1000 s in this case). This cycle can be compared directly with the laboratory results in P74, who calculated the diagnostics using observations at a single vertical level. Their Figs. 17–19 are

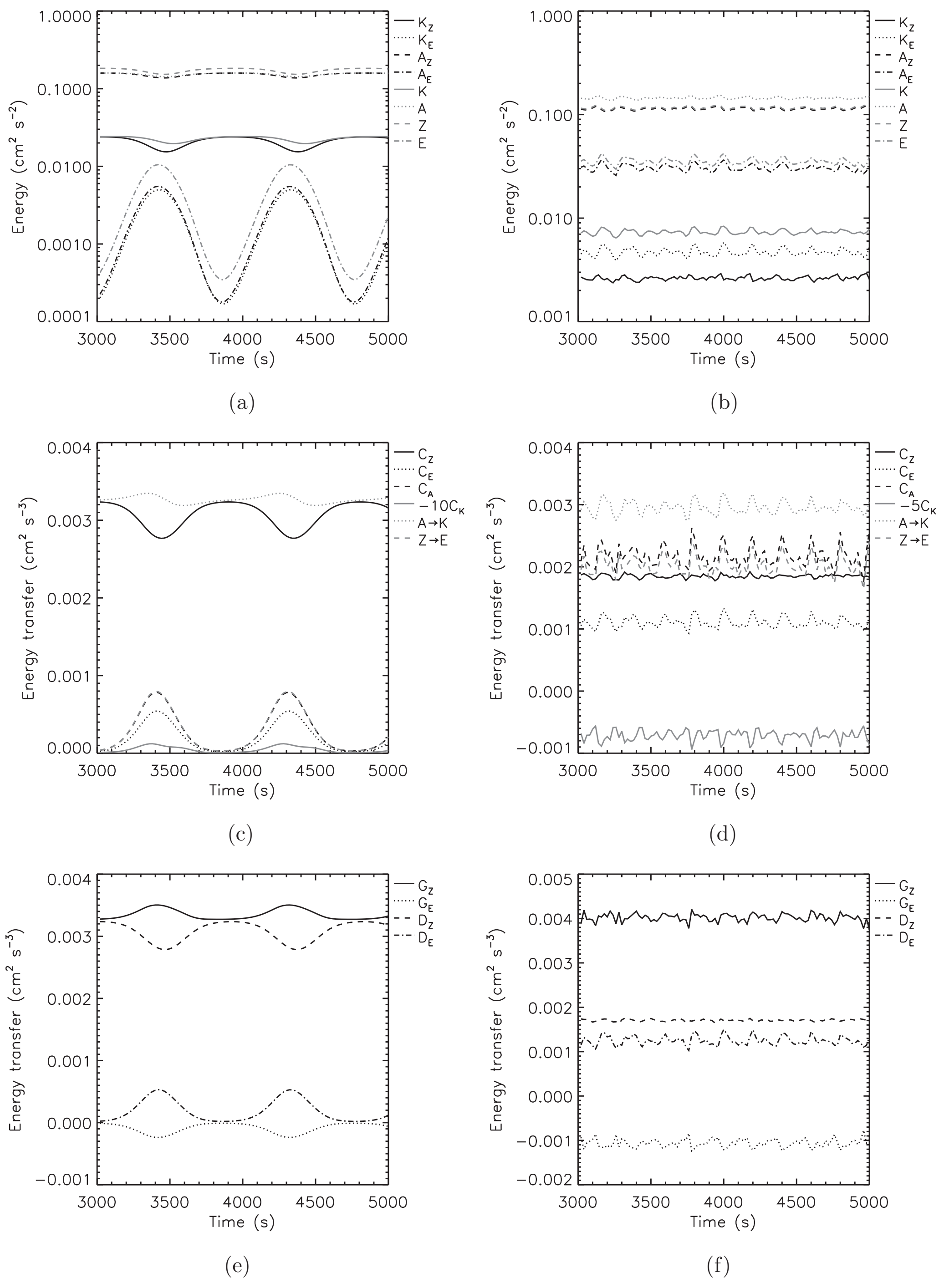

FIG. 5. Energy types and energy transfer time series. Note the y-axis scale is different for the C_K lines in (c) and (d), and the sign is reversed for direct comparison with P74. (a) 2AV energy types. (b) 3SV energy types. (c) 2AV internal energy transfers (cf. P74 Fig. 19). (d) 3SV internal energy transfers. (e) 2AV external energy transfers. (f) 3SV external energy transfers.

of particular interest, and equivalent plots are presented in Figs. 6(a), 6(c), and 5(c), respectively. In general they are qualitatively similar, with a few notable differences.

Figure 6(a) shows the available potential energy diagnostics (compare P74 Fig. 17). As in the experiments, the eddy potential energy A_E and the conversion term C_A are almost completely in phase, with A_E slightly lagging behind, as might be expected as energy is transferred to it by the

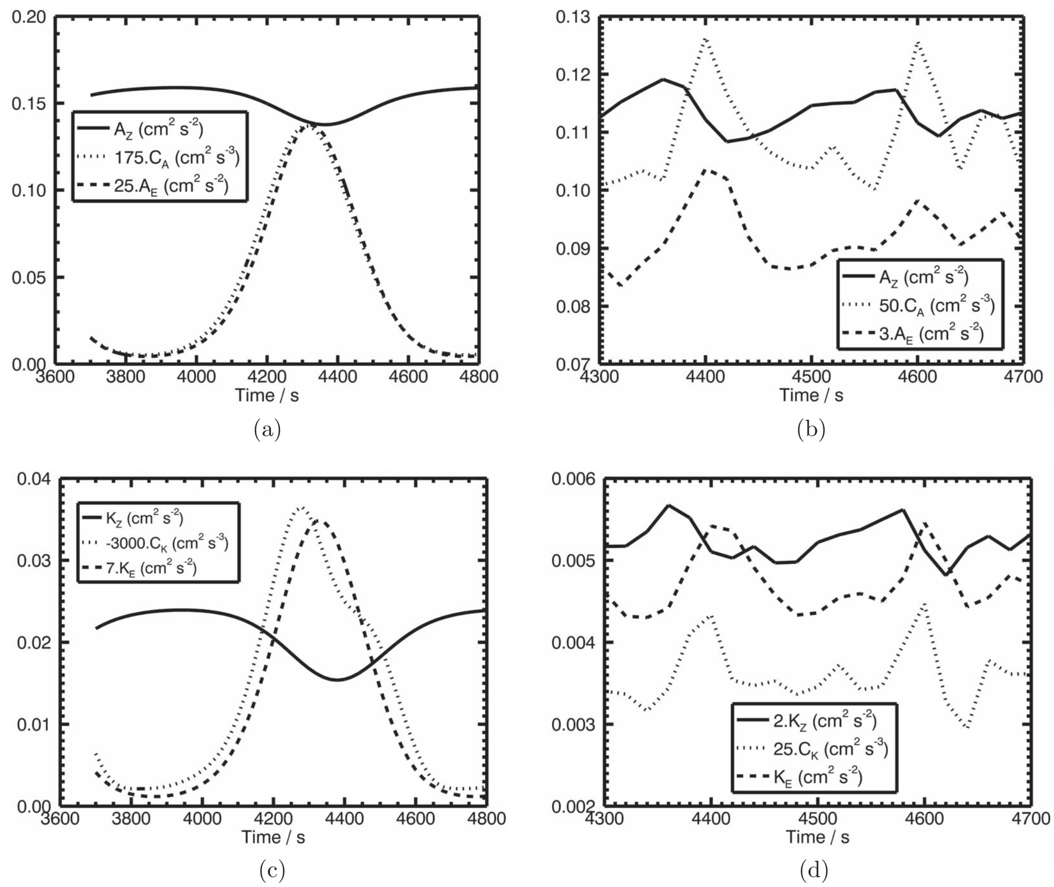

FIG. 6. Details from the 2AV and 3SV time series in Fig. 5 presented as equivalent plots to Figs. 17 and 18 in P74. (a) 2AV potential energy diagnostics (cf. P74 Fig. 17). (b) 3SV potential energy diagnostics (cf. P74 Fig. 17). (c) 2AV kinetic energy diagnostics (cf. P74 Fig. 18). Note C_K has a minus sign for direct comparison with P74. (d) 3SV kinetic energy diagnostics (cf. P74 Fig. 18).

conversion term. The phases of the cycles in these two terms relative to the cycle of zonal potential energy A_Z also agree well with experiment, with the peak in A_E lagging the peak in A_Z by about 150°. The ratio of A_E to C_A is about seven, similar to the experiments. The main difference between the experiment and simulation is the large absolute difference in the ratio between A_Z and A_E (typically 15 ± 10 in the experiment but 150 in the simulations). This might be explained by noting that the contributions to A_Z in the simulations are primarily from close to the sidewall boundary layers, which were not resolved in the experiments. Figure 7 shows the contributions to the different energy types from the various points in the fluid.

A comparison between simulation and experiment is more difficult for the kinetic energy diagnostics, because the experimental data are quite noisy. Nevertheless some comparisons can be made using Fig. 6(c) (compare P74 Fig. 18). In the simulation, the troughs in K_E and C_K occur at approximately the same time, around 3800–3900 s. The peak in K_Z then lags slightly behind this, followed by the peak in C_K, the peak in K_E, and finally the trough in K_Z. The order of peaks and troughs in K_Z, K_E, and C_K, and the phase differences between them, is more or less the same in the experiment. The agreement between simulation and experiment in such a sequence of diagnostics is encouraging. The main difference between simulation and experiment is in the ratio between K_Z and K_E, which is larger in the simulation (typically 25, but 2 ± 1 in the experiments). This is possibly the result of large velocities at the top and bottom of the tank relative to mid-height in the simulation (Fig. 7(g)). These were not measured in the P74 experiments as their thermistor array was located at mid-height.

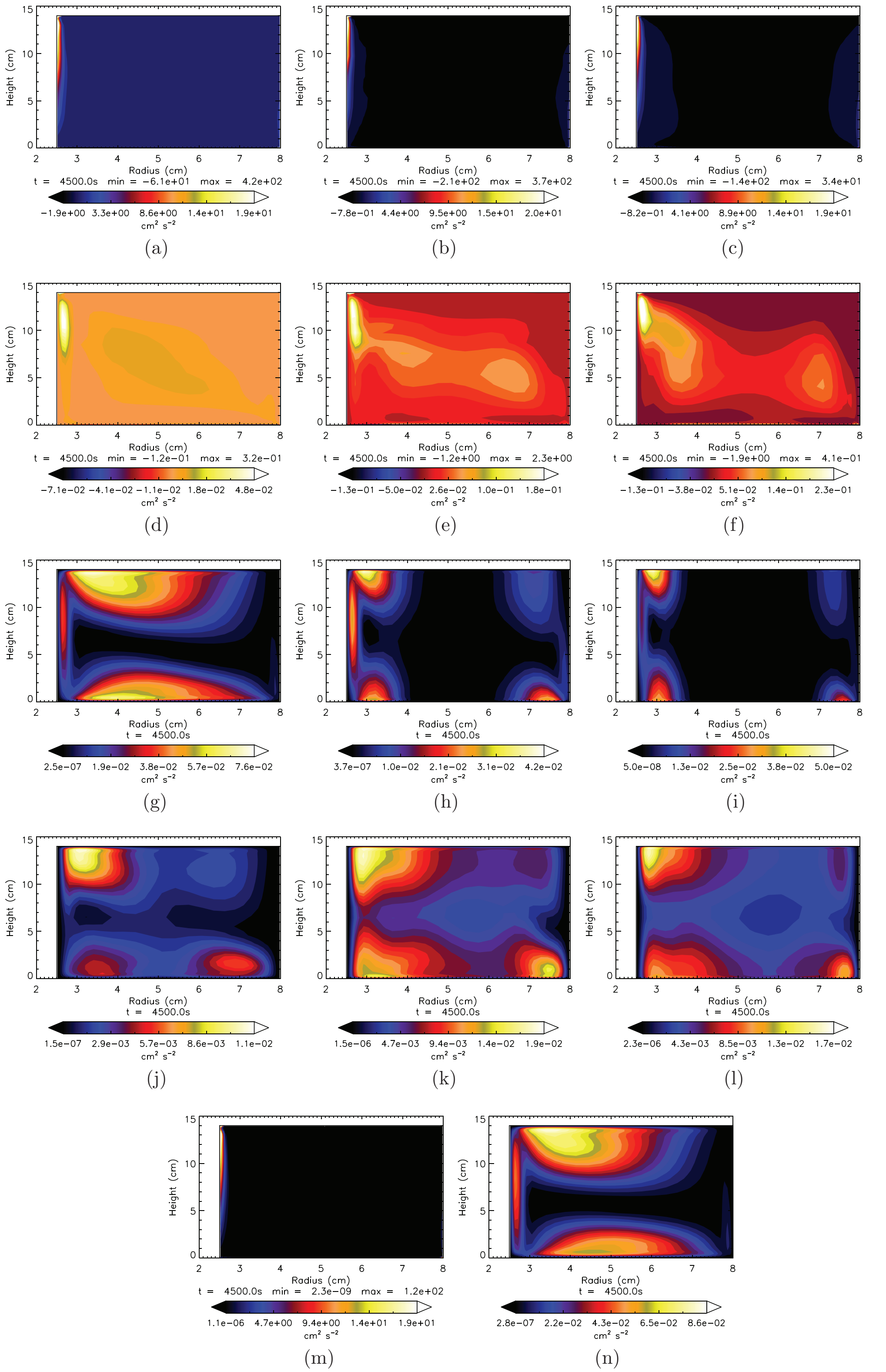

FIG. 7. Contributions to the four energy types as functions of position in the (R, z) plane at $t = 4500$ s. Where max and min are specified, the colour scale itself is restricted to the 1-99th percentiles, to improve contrast. The bottom row shows contributions to A_Z and K_Z in the AX flow at 4500 s. A_E and K_E are small for AX (within floating point precision of zero). (a) 2AV A_Z. (b) 3S A_Z. (c) 3SV A_Z. (d) 2AV A_E. (e) 3S A_E. (f) 3SV A_E. (g) 2AV K_Z. (h) 3S K_Z. (i) 3SV K_Z. (j) 2AV K_E. (k) 3S K_E. (l) 3SV K_E. (m) AX A_Z. (n) AX K_Z.

Finally, the energy conversions in P74 Fig. 19 can be compared with Fig. 5(c) here. There are some similarities but also a few differences. The phases of the four conversion terms are the same in both simulation and experiment: the peaks of C_E and C_A coincide with the trough of C_Z, all of which lag slightly behind the peak in C_K. The kinetic energy conversion term C_K is considerably smaller than the other three terms, as in the experiment. However, there are two differences worth noting. First, in the experiment $C_E > C_A$, while in the simulation $C_A > C_E$. Second, in the experiment C_Z is close to zero and negative at some points in the cycle, while in the simulation it is strongly positive at all times.

These differences might be explained by considering the contributions to the conversion terms from different points in the fluid, compared with the regions observed in the experiment. Figure 8 shows contributions to all the energy conversion terms as a function of position. The contributions to C_A and C_E at $t = 4500$ s in the 2AV case are shown in Figs. 8(d) and 8(g), and contributions to C_Z in Fig. 8(a). In the C_A term, most of the contributions come from near the top of the annulus near the inner cylinder, while the mid-height contributions are relatively small. In the C_E term there are large contributions from both mid-height and from the inner cylinder. P74 would not have captured the large contribution to C_A near the inner cylinder, and hence one expects the simulated ratio $C_A : C_E$ to be larger than it is in the experiments.

In the C_Z term, most of the contributions come from near the inner and outer cylinders, because of the strong vertical flow associated with the boundary layers. This gives a strong positive correlation between $\overline{w}''$ and $\overline{T}''$ near the inner and outer cylinders (Fig. 9). There is a negative correlation associated with a counter-circulation in the interior of the fluid (Fig. 9(b) and P74 Fig. 21), but this is much weaker than the primary overturning circulation near the boundary layers.

Some of these discrepancies can be explained by considering just the regions of the simulated fluid that were observed in the experiments. The calculations for the 2AV simulation were repeated, but restricting the vertical domain to the two grid points straddling mid-height. The radial domain was restricted by estimating the sidewall boundary layer thickness[20] for the P74 experiment (approximately 0.09 cm) compared with the distance from the sidewalls to the first thermistor (0.28 cm). The equivalent boundary layer thickness was calculated for the simulation, and a distance from each sidewall corresponding to the same ratio (three) was omitted from the integration. Figure 10 shows time series of the various energy exchanges, as in Figs. 6(a), 6(c), and 5(c), and equivalent to P74 Figs. 17–19, respectively. The peaks and troughs are in the same relative positions as in the full simulated domain and the experiment, except C_K, which is now approximately in phase with K_E rather than preceding it. Both the ratios $A_Z : A_E$ ($\sim$50) and $K_Z : K_E$ ($\sim$15) are closer to their experimental values, but the discrepancy is still quite large. The internal energy transfers (Fig. 10(c)) look much more like in P74 Fig. 19: all are in the same relative phase as the experiment and C_Z is now both positive and negative during the vacillation cycle. The only difference is that $C_A - C_E$ is marginally positive in the simulation, but negative in the experiment. Overall, the similarities between simulation and experiment are encouraging. It should be noted that the fluid used by P74 is quite different to that used here (compare $Pr = 57$ in P74 with $Pr = 13.4$ here). Differences in Prandtl number tend to have quite a large effect on the behaviour of the annulus in different flow regimes (compare Hignett *et al.*,[14] who used a fluid very similar to this work, and Früh and Read,[21] who used a fluid with $Pr = 26.7$ and saw types of behaviour not observed in the low-Pr fluid). Hence it is not to be expected that all the ratios should match the experiment.

2. Structural vacillation

There is some structure in the 3SV energy transfers, albeit not as strong a signal as in the 2AV flow. Figures 6(b) and 6(d) show the equivalent plots to Figs. 6(a) and 6(c) for the 3SV flow. Because of the shorter vacillation period (200 s) and more irregular appearance of the flow, these diagnostics are noisier, but trends can be identified. The available potential energy diagnostics (Figs. 6(a) and 6(b)) are similar in the two regimes. C_A and A_E are in phase, and the peaks of both lag behind the peak in A_Z, as in the 2AV case. Similarly, the trough in A_Z occurs just after the peaks in A_E and C_A.

In the kinetic energy diagnostics (Fig. 6(d)), the peak in K_E seems to coincide with the trough in K_Z, which is the same as for 2AV, although the exact position of the trough in K_Z is not clear for

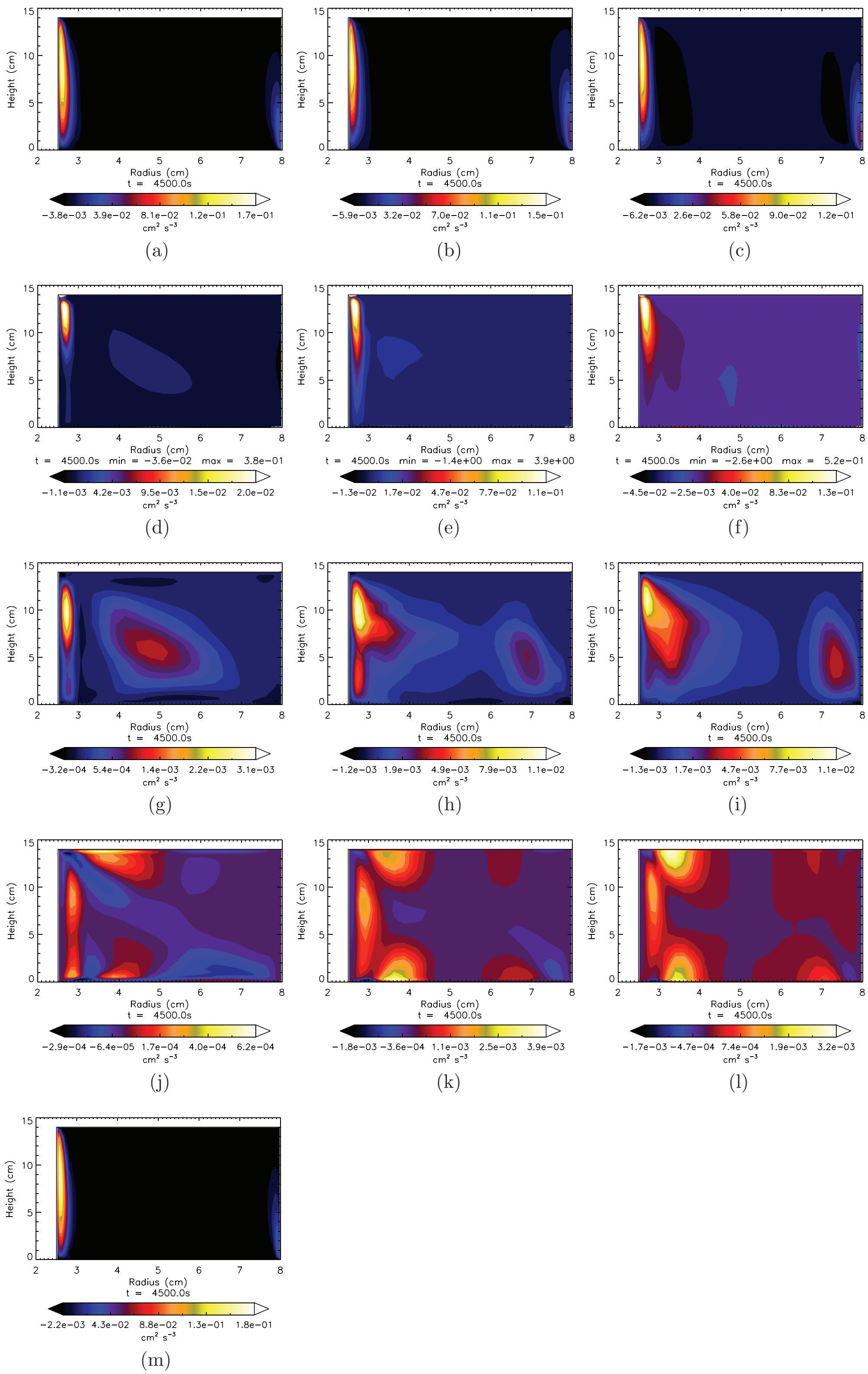

FIG. 8. Contributions to the energy conversion terms as functions of position in the (R, z) plane at $t = 4500$ s. The bottom row shows contributions to the AX C_Z conversion term as a function of position in the (R, z) plane at $t = 4500$ s. C_A, C_E, and C_K are small for AX (within floating point precision of zero). (a) 2AV C_Z. (b) 3S C_Z. (c) 3SV C_Z. (d) 2AV C_A. (e) 3S C_A. (f) 3SV C_A. (g) 2AV C_E. (h) 3S C_E. (i) 3SV C_E. (j) 2AV C_K. (k) 3S C_K. (l) 3SV C_K. (m) AX C_Z.

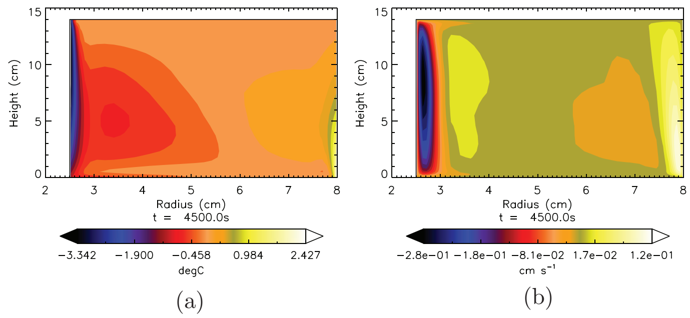

FIG. 9. Zonal mean deviations from the horizontal means for temperature and vertical velocity at $t = 4500$ s in the 2AV flow. (a) $\overline{T}''$. (b) $\overline{w}''$.

3SV. The peak in K_E lags behind the peak in C_K, which lags behind the peak in K_Z. This is the same order as the 2AV case.

The only substantive difference between these plots is that in the 3SV case C_K is positive (i.e., weak kinetic energy transfer from the mean flow to the eddies). The 3S case also has positive C_K. This term appears to depend primarily on Ω: additional runs showing 2S flow at 0.8 rad s^{-1} and 4AV flow at 1.1 rad s^{-1} showed an increasing trend in C_K with Ω, both with positive C_K. The main difference in the contributions to the C_K term between low and high Ω is that at high Ω there is a strongly positive contribution to C_K near the bottom boundary in the $-R\overline{u'v'}\partial(\overline{v}/R)/\partial R$ term, which is much weaker in the low rotation (2AV) case (see figures in the supplementary material[23]). This may be sufficient to reverse the sign of the C_K term. Ukaji and Tamaki[6,8,9] found this trend in their simulations for the free-slip upper surface case. They interpreted structural vacillation as baroclinic waves affected by a weak barotropic instability due to the positive $K_Z \to K_E$ term.[7] In their spectral analysis of steady waves[9] they found at low Ω that kinetic energy went from the dominant wave to the mean flow (i.e., $C_K < 0$), but this was reversed at moderate and high Ω, as seen here.

Held and Andrews[22] also examined the direction of energy transfer due to barotropic instability. In general they found that, with some exceptions, when the deformation radius L_D exceeded a jet's horizontal length scale L, the sense of momentum flux transfer was out of the jet (i.e., $C_K > 0$). When $L > L_D$, the momentum flux was into the jet ($C_K < 0$). The deformation radii and jet horizontal length scales were estimated for the three non-axisymmetric simulations. The deformation radius is $L_D = NH/f$, where $f = 2\Omega$, $H = d$ is a vertical length scale, and $N^2 = -(g/\rho)(d\rho/dz) \approx -g\rho_1 \Delta T/d$ is the Brunt-Väisälä frequency, using the equation of state for MORALS written down in Young and Read[13] with $\rho_1 = -3.07 \times 10^{-4}{}^\circ\mathrm{C}^{-1}$. L_D is then approximately $\sqrt{-g\rho_1\, d\, \Delta T/(4\Omega^2)}$. The jet scale was estimated by calculating the horizontal full width at half maximum (FWHM) of the jets from the zonal mean azimuthal velocity fields (included in the supplementary material;[23] these are similar in appearance to the K_Z fields in Fig. 7). These diagnostics are presented in Table IV. In the 2AV and 3S cases, the signs of $L - L_D$ and C_K do not match, which agrees with the theory in Held and Andrews,[22] but in the 3SV case the signs agree. As the jet scale and the deformation radius are quite close to each other in each case, however, it is unclear whether the measured differences between L and L_D are significant enough to provide evidence for or against Held and Andrews,[22] general result.

C. Trends in contributions to the energy diagnostics as a function of position

Some general statements can be made about how contributions to the energy types and conversions from various points in the fluid vary over the runs (Figs. 7 and 8). Additional runs showed these differences are primarily trends with Ω, however, rather than properties of the flow regimes. For the available potential energy diagnostics, most of the contributions come from close to the inner cylinder for A_Z (Figs. 7(a)–7(c), 7(m)), C_Z (Figs. 8(a)–8(c), 8(m)), and C_A (Figs. 8(d)–8(f)). There are no major differences between the flow regimes.

The vertical structure of the flow changes considerably as Ω increases between the regimes (Figs. 1(e)–1(h)). In the AX case there is a single overturning cell, but this splits into two cells in

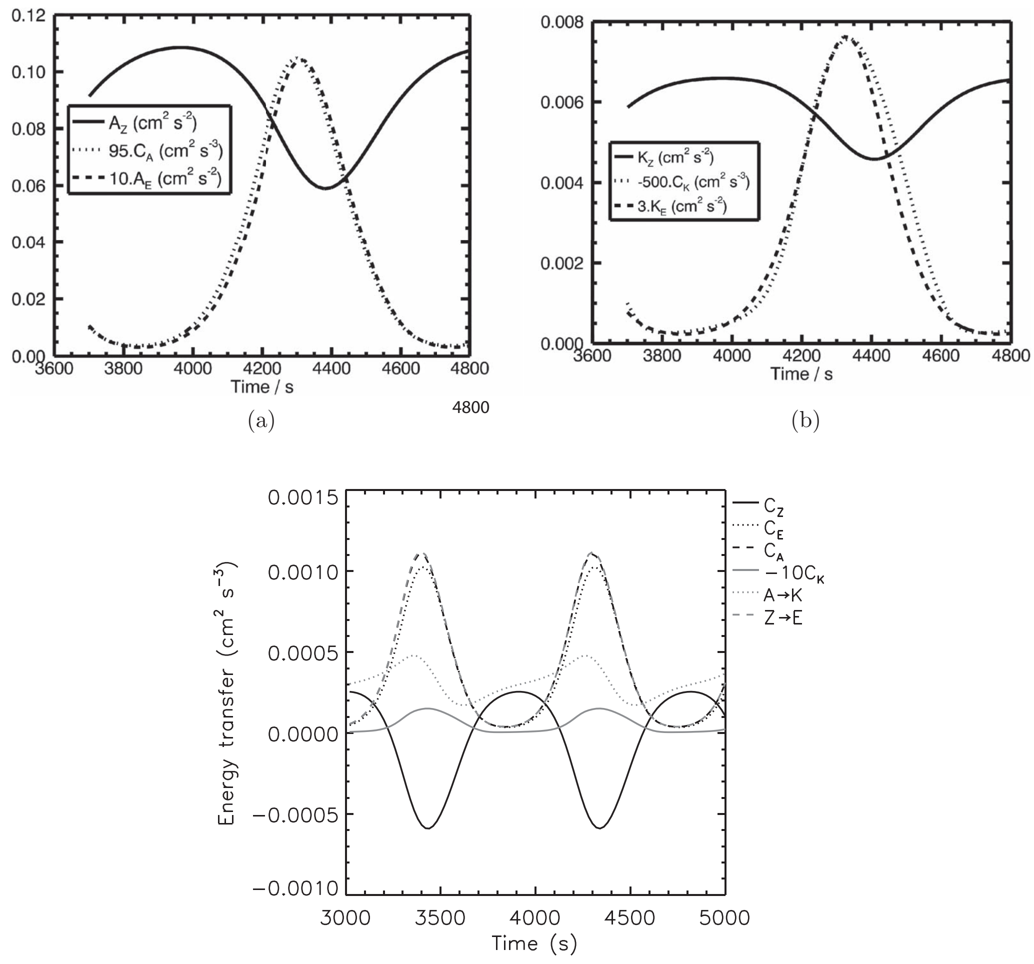

FIG. 10. Energy transfer time series for the 2AV simulation, considering only the grid points that would have been observed in the P74 experiment. (a) 2AV potential energy diagnostics (cf. Fig. 6(a) and P74 Fig. 17). (b) 2AV kinetic energy diagnostics (cf. Fig. 6(c) and P74 Fig. 18). (c) 2AV internal energy transfers (cf. Fig. 5(c) and P74 Fig. 19). Note the sign of C_K is reversed for direct comparison with P74.

the 2AV flow with a weak thermally indirect circulation between them, somewhat akin to the Ferrel cell in the Earth's zonal mean meridional circulation (e.g., Read,[10] Fig. 1(c)). The 3S and 3SV cases have clear thermally indirect circulations, with their widths becoming larger as Ω increases. The 3S case is most similar to the flow presented schematically in P74 (their Fig. 21). The strength of the thermally indirect flow is primarily a function of Ω, rather than regime, which can be seen by

TABLE IV. Zonal jet scale diagnostics at $t = 4500$ s for the three non-axisymmetric flows. The values given for L are the averages and standard deviations of the horizontal FWHM over all the jets in the domain for a particular flow (two for 2AV, four for 3S and 3SV).

Flow regime	2AV	3S	3SV
Zonal jet scale L (cm)	4.5 ± 0.2	1.2 ± 0.2	0.9 ± 0.1
Deformation radius L_D (cm)	3.9	1.5	0.68
Does $L > L_D$?	✓	✗	✓
Does $C_K < 0$ (Fig. 4)?	✓	✗	✗
Agreement with Held and Andrews[22]?	✓	✓	✗

examining the kinetic energy diagnostics. The main difference between the regimes comes in the kinetic energy diagnostics, particularly K_Z. The AX and 2AV flows have single maxima in K_Z near the top and bottom of the annulus (Figs. 7(n) and 7(g)), while there are two maxima at the top and bottom of the tank in the 3S and 3SV cases (Figs. 7(h) and 7(i)). This is driven mainly by the differences in zonal mean azimuthal velocity, which are split into two maxima for 3S and 3SV but only exhibit a single maximum for AX and 2AV, while contributions from zonal mean radial and vertical velocities are the same in each case. Compare this with Fig. 9(b)[top] in Ukaji and Tamaki,[8] which shows a difference between the no-slip and free-slip cases—there are no peaks in $\overline{v}$ near the top of the tank in that case. However, an AV simulation at higher rotation rate (1.1 rad s^{-1}) had two maxima in K_Z near the top, indicating that this is a function of rotation rate rather than a property of the flow regime.

This difference is not so pronounced in the K_E field (Figs. 7(j)–7(l)), where all flow regimes have two maxima at the top and bottom (except AX, where there are no eddies at all).

D. Energy cycles at the extremes of the 2AV vacillation cycle

The energy transfers vary considerably over the course of a single amplitude vacillation cycle. In this particular 2AV run, $t = 4320$ s is the point in one cycle when the eddies are strongest, and 4780 s the point when the eddies are weakest. Figure 11 shows the basic appearance of the flow at these two extremes and the corresponding energy cycles. Fig. 1(b) at 4500 s is approximately halfway between these two extremes. There is a considerable difference in the appearance of the flow at these times.

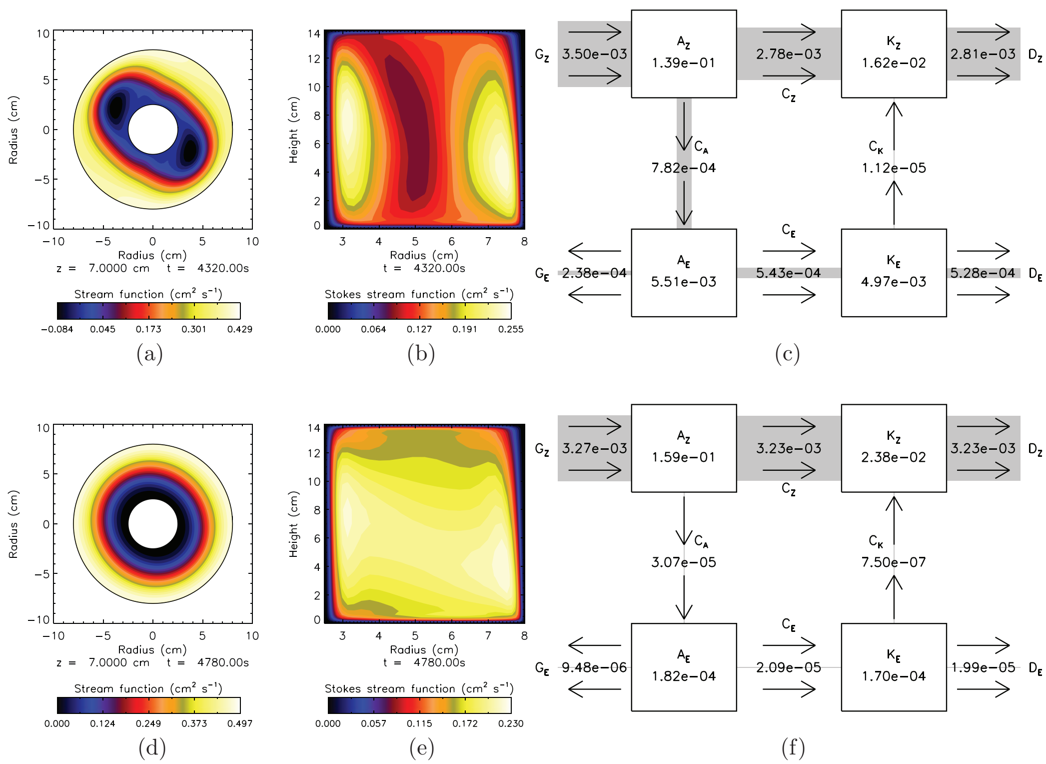

FIG. 11. Basic appearance of the 2AV flow and energy cycles at the points in the vacillation cycle where eddies are strongest (4320 s, top row) and weakest (4780 s, bottom row). All energy types in (c) and (f) (in boxes) are in cm^2 s^{-2} ($\equiv 10^{-4}$ J kg^{-1}) and all energy transfers (arrows) are in cm^2 s^{-3} ($\equiv 10^{-4}$ W kg^{-1}). The streamfunctions are defined as in Fig. 1. (a) Horizontal stream function at 4320 s. (b) Meridional (Stokes) stream function at 4320 s. (c) Energy cycle at 4320 s. (d) Horizontal stream function at 4780 s. (e) Meridional (Stokes) stream function at 4780 s. (f) Energy cycle at 4780 s.

At 4320 s the eddy fields are strongest, corresponding to the largest baroclinic wave amplitude. The thermally indirect circulation in the middle of the vertical cross-section is now clear (Fig. 11(b)), and stronger than at 4500 s. The baroclinic wave is not as strong as in the 3S case, where there is a clear separation between each of the cyclones and the inner cylinder (Fig. 1(c)), while in the 2AV case there is a strong front with a weaker central vortex (Figs. 1(b) and 11(a)). The energy cycle (Fig. 11(c)) also resembles the cycle for the 3S case (Fig. 4(c)), albeit with slightly weaker eddy flow and with a reversed C_K. The terms C_A and C_E are non-negligible and of the correct sign for baroclinic instability, and the ratio between the terms is comparable with the ratios in the 3S case, although the ratio $C_A : C_Z$ never reaches the value in the 3S case, with a value of only 0.28 in Fig. 11(c) compared with 0.77 for 3S. At this extreme of the amplitude vacillation cycle the flow resembles a steady baroclinic wave.

At the opposite end of the cycle at 4780 s, however, the flow is almost axisymmetric. The horizontal streamfunction (Fig. 11(d)) is almost axisymmetric, like the AX case (Fig. 1(a)), and the 2AV Stokes stream function (Fig. 11(e)) is very similar to the AX case (Fig. 1(e)), with a single primary meridional overturning circulation. The energy cycle (Fig. 11(f)) is also akin to the axisymmetric case presented in Fig. 4(a), with almost all the energy transfer in G_Z, C_Z, and D_Z. However, it should be noted that, compared with the AX case, the eddy energy fluxes remain distinctly non-zero, even when the flow looks axisymmetric.

Figure 11 shows clearly that over the course of a single amplitude vacillation cycle the energy exchanges and flow appearance vary between those associated with baroclinic instability, and those associated with an overturning (Hadley-type) circulation.

V. CONCLUSION

This paper has presented the components of the Lorenz energy cycle for a number of simulated rotating annulus flows. Simulating the rotating annulus allows more detail about energy transfers to be obtained than is possible with experiments, because the model allows access to unobserved parts of the flow, particularly in the vertical plane.

The four flow regimes simulated here showed a variety of energy characteristics associated with two of the energy cycle paradigms listed by James[2] (his Fig. 5.14). A Hadley-type axisymmetric meridional overturning circulation associated with positive G_Z, C_Z, and D_Z was found in the AX simulation and at the low-amplitude extreme of the 2AV vacillation cycle. Baroclinic instability associated with positive G_Z, C_A, and C_E was found with various magnitudes in the 3S and 3SV cases, and at the high-amplitude extreme of the 2AV vacillation cycle. Barotropic instability, associated with positive C_K, was not dominant in any of the flows, but increased in strength as the rotation rate increased.

The correspondence between the simulations and experiments in P74 was encouraging, with the energy cycles in the 2AV flow matching well, particularly when only the region of the flow observed by P74 was considered. There was a good correspondence between the diagnostics obtained in the 3S and 3SV simulations and in Lorenz's[1] original estimates of various ratios for Earth's mid-latitudes, such as the ratio between C_A and C_K, and the ratio between G_Z and C_A. These two simulations have thermal Rossby numbers comparable with Earth's mid-latitudes, again demonstrating that the differentially heated rotating annulus is a useful laboratory analogue for many of the salient features of large-scale flow in an Earth-like planetary atmosphere.[23]

ACKNOWLEDGMENTS

I thank Richard Pfeffer for all his help with the expressions for the energy diagnostics, and for identifying an error in one of his equations. Peter Read kindly proofread the manuscript before submission and provided some useful comments. Two anonymous reviewers made a number of useful comments that improved the manuscript. Many of the figures used David Fanning's Coyote IDL Program Library. This work was supported by UK Science & Technology Facilities Council grants ST/I001948/1 and ST/K00106X/1, and was supported in part by the US National Science Foundation under Grant No. NSF PHY11-25915.

[1] E. N. Lorenz, "Available potential energy and the maintenance of the general circulation," Tellus **7**, 157–167 (1955).
[2] I. N. James, *Introduction to Circulating Atmospheres*, 1st ed. (Cambridge University Press, Cambridge, UK, 1994), p. 422.
[3] J. R. Holton, *An Introduction to Dynamic Meteorology*, 4th ed. (Elsevier Academic Press, Burlington, MA, USA, 2004), p. 535.
[4] R. L. Pfeffer and Y. Chiang, "Two kinds of vacillation in rotating laboratory experiments," Mon. Weather Rev. **95**, 75–82 (1967).
[5] R. Pfeffer, G. Buzyna, and W. W. Fowlis, "Synoptic features and energetics of wave-amplitude vacillation in a rotating, differentially-heated fluid," J. Atmos. Sci. **31**, 622–645 (1974).
[6] K. Ukaji and K. Tamaki, "A comparison of laboratory experiments and numerical simulations of steady baroclinic waves produced in a differentially heated rotating fluid annulus," J. Meteorol. Soc. Jpn. **67**, 359–374 (1989), available at https://www.jstage.jst.go.jp/article/jmsj1965/67/3/67_3_359/_article.
[7] K. Ukaji and K. Tamaki, "A numerical study of tilted-trough vacillation observed in a differentially heated rotating fluid annulus," J. Meteorol. Soc. Jpn. **68**, 447–460 (1990), available at https://www.jstage.jst.go.jp/article/jmsj1965/68/4/68_4_447/_article.
[8] K. Ukaji and K. Tamaki, "A numerical study of amplitude vacillation observed in a differentially heated rotating fluid annulus," J. Meteorol. Soc. Jpn. **72**, 1–10 (1994), available at https://www.jstage.jst.go.jp/article/jmsj1965/72/1/72_1_1/_article.
[9] K. Ukaji and K. Tamaki, "A numerical study of steady baroclinic annulus waves: Wave drift rates and energetics," J. Meteorol. Soc. Jpn. **77**, 639–647 (1999), available at https://www.jstage.jst.go.jp/article/jmsj1965/77/3/77_3_639/_article.
[10] P. L. Read, "Dynamics and circulation regimes of terrestrial planets," Plan. Space Sci. **59**, 900–914 (2011).
[11] R. Hide and P. J. Mason, "Sloping convection in a rotating fluid," Adv. Phys. **24**, 47–100 (1975).
[12] R. L. Pfeffer, G. Buzyna, and R. Kung, "Time-dependent modes of behavior of thermally driven rotating fluids," J. Atmos. Sci. **37**, 2129–2149 (1980).
[13] R. M. B. Young and P. L. Read, "Data assimilation in the laboratory using a rotating annulus experiment," Q. J. Roy. Meteorol. Soc. **139**, 1488–1504 (2013).
[14] P. Hignett, A. A. White, R. D. Carter, W. D. N. Jackson, and R. M. Small, "A comparison of laboratory measurements and numerical simulations of baroclinic wave flows in a rotating cylindrical annulus," Q. J. Roy. Meteorol. Soc. **111**, 131–154 (1985).
[15] P. L. Read, N. P. J. Thomas, and S. H. Risch, "An evaluation of Eulerian and semi-Lagrangian advection schemes in simulations of rotating, stratified flows in the laboratory. Part I: Axisymmetric flow," Mon. Weather Rev. **128**, 2835–2852 (2000).
[16] Richard Pfeffer, personal communication (2013). In P74 Eq. (7) there is a typo—an erroneous $''$ on the $\overline{T'u'}$ term, i.e., it was written $\overline{T'u'}''$ (NB: different notation). The corrected version is consistent with both Lorenz[1] Eq. (26) and James[2] Fig. 5.13, while the P74 Eq. (7) expression is not.
[17] Some integrals involved $(\partial\tilde{T}/\partial z)^{-1}$ terms, but $\partial\tilde{T}/\partial z$ can cross zero in the endwall boundary layers. Where $\partial\tilde{T}/\partial z$ was very small ($<10^{-3\circ}$ C cm^{-1}) the grid point was removed and adjacent grid points in the column redefined so the whole column was still integrated over, but avoiding grid points where $(\partial\tilde{T}/\partial z)^{-1}$ was very large.
[18] Thermal Rossby number $Ro_T = g\alpha\Delta Td/(\Omega^2(b-a)^2)$. Using data from Andrews[19] atmospheric scale height $d \approx 7.6$ km (p. 26), $\Delta T \approx 25$ K between latitude boundaries of 30° N and 60° N, mean surface temperature at same latitudes ≈280 K (used for $\alpha_v = 1/T$) (both Fig. 1.5), surface gravity $g = 9.81$ m s^{-2}, mean planetary radius = 6371 km (for $b - a$), and $\Omega = 7.29 \times 10^{-5}$ rad s^{-1} (all Appendix 1).
[19] D. G. Andrews, *An Introduction to Atmospheric Physics* (Cambridge University Press, Cambridge, UK, 2000), p. 229.
[20] The sidewall (Stewartson) boundary layer thickness is given by $l_S = \min[(b-a)Ek^{1/3}, d/S^{1/4}]$, where $Ek = \nu/(\Omega d^2)$ is the Ekman number, and $S = |\alpha g\Delta T|d^3/(\nu\kappa)$ is the Stewartson number, ν is kinematic viscosity, κ thermal diffusivity, and α the volume expansion coefficient, using values listed in Young and Read.[13]
[21] W.-G. Früh and P. L. Read, "Wave interactions and the transition to chaos of baroclinic waves in a thermally driven rotating annulus," Philos. T. R. Soc. London A **355**, 101–153 (1997).
[22] I. M. Held and D. G. Andrews, "On the direction of the eddy momentum flux in baroclinic instability," J. Atmos. Sci. **40**, 2220–2231 (1983).
[23] See supplementary material at http://dx.doi.org/10.1063/1.4873921 for intermediate fields used to calculate the energy types and energy transfers in Eqs. (1)–(8), plus a few additional time series.